



# Towards the improvement of methane production in CO<sub>2</sub> photoreduction using Bi<sub>2</sub>WO<sub>6</sub>/TiO<sub>2</sub> heterostructures

Laura Collado<sup>a,\*</sup>, Miguel Gomez-Mendoza<sup>a</sup>, Miguel García-Tecedor<sup>a</sup>, Freddy E. Oropeza<sup>a</sup>, Anna Reynal<sup>b,c</sup>, James R. Durrant<sup>b,c</sup>, David P. Serrano<sup>d,e,\*\*</sup>, Víctor A. de la Peña O'Shea<sup>a,\*</sup>

<sup>a</sup> Photoactivated Processes Unit, IMDEA Energy Institute, Parque Tecnológico de Móstoles, Avda. Ramón de la Sagra 3, 28935 Móstoles, Madrid, Spain

<sup>b</sup> SPECIFIC IKC, College of Engineering, Swansea University, Swansea SA1 8EN, UK

<sup>c</sup> Department of Chemistry and Centre for Processable Electronics, Molecular Sciences Research Hub, Imperial College London, London W12 0BZ, UK

<sup>d</sup> Department of Chemical and Environmental Technology, ESCET, Universidad Rey Juan Carlos, C/ Tulipán s/n, 28933 Móstoles, Madrid, Spain

<sup>e</sup> Thermochemical Processes Unit, IMDEA Energy Institute, Parque Tecnológico de Móstoles, Avda. Ramón de la Sagra 3, 28935 Móstoles, Madrid, Spain

## ARTICLE INFO

### Keywords:

CO<sub>2</sub> photoreduction  
Bi<sub>2</sub>WO<sub>6</sub>/TiO<sub>2</sub> heterojunction  
CH<sub>4</sub> production  
Charge dynamics studies

## ABSTRACT

Russelite bismuth tungstate (Bi<sub>2</sub>WO<sub>6</sub>) has been widely reported for the photocatalytic degradation and mineralization of a myriad of pollutants as well as organic compounds. These materials present perovskite-like structure with hierarchical morphologies, which confers excellent optoelectronic properties as potential candidates for photocatalytic solar fuels production. Here, we propose the development of Bi<sub>2</sub>WO<sub>6</sub>/TiO<sub>2</sub> heterojunctions for CO<sub>2</sub> photoreduction, as a promising solution to produce fuels, alleviate global warming and tackle fossil fuel shortage. Our results show an improvement of the photocatalytic activity of the heterojunctions compared to the pristine semiconductors. Near Ambient Pressure X-ray Photoelectron Spectroscopy (NAP-XPS) experiments reveals a preferential CO<sub>2</sub> adsorption over TiO<sub>2</sub>. On the other hand, transient absorption spectroscopy measurements show that the charge transfer pathway in Bi<sub>2</sub>WO<sub>6</sub>/TiO<sub>2</sub> hybrids leads to longer-lived photogenerated carriers in spatially separated redox active sites, which favor the reduction of CO<sub>2</sub> into highly electron demanding fuels and chemicals, such as CH<sub>4</sub> and C<sub>2</sub>H<sub>6</sub>.

## 1. Introduction

The large amounts of anthropogenic CO<sub>2</sub> emissions, primarily from the burning of fossil fuels, are leading to a devastating impact on global climate and health. In this scenario, the development of sustainable and efficient carbon-neutral energy technologies is critical to address the harmful effects of greenhouse gases while fulfilling the future energy demand [1,2]. Sunlight plays a critical role in the development of emerging sustainable energy conversion and storage technologies [3]. Light-matter interactions govern a large number of important photochemical and photophysical processes that ultimately determine the existence of life on the Earth, such as natural photosynthesis [4]. One of the most promising energy conversion strategies is to mimic natural photosynthesis by converting sunlight into fuels and valuable chemicals, using abundant feedstocks like water and carbon dioxide [5,6]. If developed at industrial scale, this artificial photosynthesis approach

would have the potential to significantly substitute fossil fuels and reduce CO<sub>2</sub> emissions.

Nevertheless, the activation of the stable CO<sub>2</sub> molecule is one of the biggest challenges in chemistry, which necessarily requires the rational design of high-performance photocatalysts [7]. In general terms, photocatalytic activity is closely related to the structural properties of the catalyst and its electronic band structure. Aurivillius-based compounds characteristically form hierarchical structures with specific morphology and high order, which are interesting for catalytic applications and structure-reactivity studies. Among them, bismuth tungstate (Bi<sub>2</sub>WO<sub>6</sub>) is the simplest member of this oxide family and perhaps the most studied example for photocatalytic applications [8,9]. This material presents a perovskite-like structure with corner-sharing WO<sub>6</sub> octahedrons sandwiched between (Bi<sub>2</sub>O<sub>2</sub>)<sup>2+</sup> layers, which confers excellent optoelectronic properties and an appropriate bandgap for multitude of photocatalytic processes [10,11]. Generally, Bi<sub>2</sub>WO<sub>6</sub> has been used to

\* Corresponding authors.

\*\* Corresponding author at: Department of Chemical and Environmental Technology, ESCET, Universidad Rey Juan Carlos, C/ Tulipán s/n, 28933 Móstoles, Madrid, Spain.

E-mail addresses: [laura.collado@imdea.org](mailto:laura.collado@imdea.org) (L. Collado), [david.serrano@imdea.org](mailto:david.serrano@imdea.org) (D.P. Serrano), [victor.delapenya@imdea.org](mailto:victor.delapenya@imdea.org) (V.A. de la Peña O'Shea).

<https://doi.org/10.1016/j.apcatb.2022.122206>

Received 8 September 2022; Received in revised form 16 November 2022; Accepted 22 November 2022

Available online 23 November 2022

0926-3373/© 2022 The Authors. Published by Elsevier B.V. This is an open access article under the CC BY-NC-ND license (<http://creativecommons.org/licenses/by-nc-nd/4.0/>).

degrade organic pollutants [12], while its application for artificial photosynthesis, and especially for CO<sub>2</sub> reduction into fuels and chemicals, has been more limited to date [13]. An interesting strategy to increase the separation of photogenerated charge carriers and to improve the photocatalytic efficiencies is the development of semiconductor-based heterojunctions [14]. Among inorganic heterojunctions, coupling of Bi<sub>2</sub>WO<sub>6</sub> with a wider band-gap semiconductor, such as the benchmark TiO<sub>2</sub>, may facilitate the separation and transfer of charge carriers through the heterostructure, due to the internal field induced by the different electronic band structures [15–17]. Based on this premise, this work explores the beneficial properties of Bi<sub>2</sub>WO<sub>6</sub>/TiO<sub>2</sub> heterojunctions towards the photocatalytic production of fuels and chemicals by artificial photosynthesis. Moreover, this study presents experimental evidence for the charge dynamics and the light-induced changes on the surface chemistry of Bi<sub>2</sub>WO<sub>6</sub>/TiO<sub>2</sub> heterojunctions, which may provide valuable insights for many other catalytic and environmental applications.

## 2. Experimental

### 2.1. Synthesis procedure

Bi<sub>2</sub>WO<sub>6</sub> photocatalyst was prepared through a hydrothermal process. All chemicals used were analytic grade reagents without further purification. In a typical procedure, 2.425 g of bismuth nitrate (Bi(NO<sub>3</sub>)<sub>3</sub> • 5 H<sub>2</sub>O) and 0.907 g of sodium tungstate (Na<sub>2</sub>WO<sub>4</sub> • 2 H<sub>2</sub>O) were mixed in 80 mL Milli-Q water, according to a molar ratio WBi = 0.55. The obtained mixed solution was kept under vigorous stirring for 3 h and straightaway it was transferred to a 100 mL Teflon-lined autoclave sealed into a stainless steel tank to carry out the hydrothermal treatment at 160 °C for 20 h. Then, the reactor was let to cool down to room-temperature naturally and after that, resulting sample was collected by filtration and washed with Milli-Q to remove any rest of precursors. Finally, the solid was dried at 90 °C in air for 15 h. The resulting yellow product was ground into powder for further use. Sample was labeled as BiW.

A series of Bi<sub>2</sub>WO<sub>6</sub>/TiO<sub>2</sub> heterojunctions were prepared using commercial TiO<sub>2</sub>-anatase PC500 (CrystalACTiV™) following a hydrothermal treatment [15]. In brief, the corresponding amount of TiO<sub>2</sub> (0.6–75 wt.% TiO<sub>2</sub>) was first dispersed in 20 mL HNO<sub>3</sub> (0.2 M) to activate the powders before use, and then sonicated for 1 h. After that, TiO<sub>2</sub> was added to the white suspension of the Bi-W precursors (molar ratio WBi = 0.55), following the procedure described above. The resulting mixture was submitted to hydrothermal treatment at 160 °C for 18 h, drying at 90 °C for 4 h and calcination in air at 400 °C for 4 h. Samples were labeled as BiW/Tix (where x: 0.6–75 wt.% TiO<sub>2</sub>).

### 2.2. General characterization

The crystal structure of Bi<sub>2</sub>WO<sub>6</sub> was characterized by X-Ray diffraction (XRD) with a diffractometer Philips PW 3040/00 X'Pert MPD/MRD, using Cu K<sub>α</sub> radiation ( $\lambda = 1.54178$  Å) and a scanning rate of 0.2° s<sup>-1</sup>. Specific surface areas were measured on a QUADRASORB instrument from N<sub>2</sub> physisorption at 77 K, after degassing samples in N<sub>2</sub> at 105 °C for 20 h. The BJH method was used to determine the pore size distribution. The morphology of the particles was observed by using a Hitachi TM-1000 Scanning Electron Microscope (SEM), operating with tungsten filament working at 15 kV, a JEOL JSM-7900 F Field Emission Scanning Electron Microscope (FESEM) equipped with an ULTIM Max 170 X-ray energy dispersive spectroscopy (X-EDS) detector, and a Philips Technai 20 Transmission Electron Microscope (TEM) with tungsten filaments operating at 200 kV. Raman spectroscopy was conducted on a Jasco NRS-5100 spectrometer (532 nm laser wavelength, 5.3 mW power). Near-ambient pressure X-ray photoelectron spectroscopy (NAP-XPS) of samples was done in a lab-based spectrometer (SPECS GmbH, Berlin) using a monochromated Al K<sub>α</sub>1 source ( $h\nu = 1486.6$  eV) at 50 W,

and a 300 μm a spot size. The samples were studied on a 180° hemispherical energy analyzer (SPECS PHOIBOS 150 NAP analyser) with 150 mm mean radius, equipped with a nozzle with a 300 μm diameter orifice. The total energy resolution of the measurements was about 0.5 eV. The binding energy (BE) was calibrated against the Fermi level (E<sub>F</sub>) of Au. For NAP experiments, samples were exposed to a 1 mbar total pressure of a 4:1 CO<sub>2</sub>:H<sub>2</sub>O mixture at room temperature. The pressure was dwelled for 15 min before taking the spectra. Ultraviolet–visible diffuse reflectance spectra (UV–Vis DRS) of powdered samples were obtained by a Perkin Elmer Lambda 1050 UV/Vis/NIR spectrometer. Quantification of the band gap transition was determined from the steep shape of the spectra and the equation  $\alpha h\nu = A(h\nu - E_g)^m$  was employed where the absorption coefficient ( $\alpha$ ) is related to the incident photon energy ( $h\nu$ ), A is constant, m is the index indicating the type of transition.

### 2.3. Theoretical calculations

Periodic density functional theory (DFT) calculations were carried out using bulk Bi<sub>2</sub>WO<sub>6</sub>. Geometry and electronic structure were carried out using Viena ab initio simulation package (VASP). The total energies of the optimized geometries were estimated using the spin polarized version of the Perdew–Burke–Ernzerhof (PBE). A more accurate energy gap was fitted using the Heyd–Scuseria–Ernzerhof hybrid functional (HSE06) with a mixing parameter of 0.25. A cut-off of 500 eV was set for the kinetic energy of the plane-waves to ensure a total energy and force convergence higher than 10<sup>-4</sup> eV and 0.01 eV/Å<sup>3</sup>, respectively.

### 2.4. Photoelectrochemical characterization

**Photoelectrodes preparation.** For the preparation of the electrodes, an ink was prepared using 5 mg of the precursor powder, 20 μl of 5 wt% Nafion solution (Sigma-Aldrich) and 1 mL of a 3:1 mixture of deionized water and isopropanol. Then the mixture is introduced in a vial, and an ultrasonic treatment is performed to ensure the homogeneity. For the photoelectrodes preparation, the ink is drop-casted on FTO (F: SnO<sub>2</sub>) covered glass substrates.

**Photoelectrochemical measurements.** Experiments were performed in a three-electrode configuration electrochemical cell, also equipped with a quartz window. Measurements were carried out using an aqueous solution of 0.5 M Na<sub>2</sub>SO<sub>3</sub>, an Ag/AgCl electrode (reference), a Pt wire (counter electrode) and the corresponding fabricated photoelectrode (working electrode). Analysis were carried out with a potentiostat-galvanostat PGSTAT204 equipped with an integrated impedance module FRAII (10 mV of modulation amplitude is used at 400 Hz). A solar simulator (LOT LSH302 Xe lamp and an LSZ389 AM1.5 global filter) calibrated as 1 Sun (100 m W/cm<sup>2</sup>) was used as the illumination source.

### 2.5. Photophysical characterization

**Steady-state and Time-Resolved Photoluminescence.** Fluorescence measurements of powdered samples were performed on a Fluorescence Spectrometer Perkin Elmer LS 55 in front-face mode, using an excitation wavelength of 300 nm and a cut-off filter at 350 nm. Time resolved fluorescence measurements of powdered samples were recorded in a Mini Tau system (Edinburgh Instruments), using an EPL-375 picosecond pulsed diode laser with fluorescence emission at  $\lambda_{exc} = 372$  nm.

**Transient Absorption Spectroscopy (TAS).** Laser flash photolysis measurements were carried out with a LP980 equipment (Edinburgh Instruments) based on an optical parametric oscillator (OPO) pumped by the third harmonic of a Nd:YAG laser (EKSPLA). Measurements were performed using an excitation wavelength of 355 nm with either single low energy pulses of 300 μJ or more energetic 2 mJ/pulse of ca. 5 ns duration. A pulsed xenon flash lamp (150 W) was employed as the detecting light source. The probe light was dispersed through a monochromator (TMS302-A, grating 150 lines/mm) and analysed on a PMT

detector (Hamamatsu Photonics) to acquire temporal profiles. The absorbance of all dispersed solutions was kept at  $\sim 0.3$  at  $\lambda_{\text{exc}} = 355$  nm. All transient spectra were recorded at room temperature using  $10 \times 10$  mm<sup>2</sup> quartz cells, after bubbling with N<sub>2</sub> for 15 min before acquisition.

## 2.6. CO<sub>2</sub> photoreduction

CO<sub>2</sub> photoreduction experiments were performed in a home-made reaction system under continuous-flow mode. The gas-phase photo-reactor (280 mL) was made of steel with a borosilicate window for irradiation. Solid catalysts (0.1 g) were deposited on a glass microfiber filter. A mixture of CO<sub>2</sub> (99.9999%, Praxair) and water vapor with a molar ratio of 7.25 (CO<sub>2</sub>:H<sub>2</sub>O) was generated in a Controller Evaporator Mixer (CEM) and fed to the reactor. UV illumination was performed using four 6 W lamps (maximum wavelength at 365 nm) with an average intensity of  $71.7 \text{ W m}^{-2}$  (measured by a Blue-Wave spectrometer in the range 330–400 nm). The reaction conditions were set at 2 bars and 50 °C. Reaction products were detected in continuous mode with a gas chromatograph (GC, Agilent 7890 A) equipped with two separation branches and two sampling loops. First separation branch contained two semicapillary columns (HP Plot Q and Molesieve 5 A), a Thermal Conductivity Detector (TCD), a Flame Ionization Detector (FID) and a methanizer. Second separation branch contained a capillary column (CP-Sil 5B) and a second Flame Ionization Detector (FID).

Prior to experiments, the reactor was degassed under vacuum at 80 °C and then purged with Ar ( $100 \text{ mL min}^{-1}$  for 1 h) to remove any residual organics weakly adsorbed on the catalyst surface. Then, the catalyst was exposed to the CO<sub>2</sub> and H<sub>2</sub>O mixture for 1 h to establish an adsorption–desorption balance. Blank experiments did not detect any product formation under dark conditions or without any catalyst under UV illumination. However, GC analyses detected small amounts of CO<sub>2</sub> ( $< 200$  ppm) in the feed composition before starting the illumination. This finding indicates that even high purity reagents may contain impurities, which could form adsorbed species (e.g. carbonates/bicarbonates) that may participate in the reaction. All tests were performed under 0–15 h of illumination, and repeated at least twice to guarantee reproducibility.

Photonic efficiency ( $\mathfrak{z}$ ) calculation. Photonic efficiencies were calculated as the ratio of reaction rate and incident photon flux, according to Eq. (1).

$$\mathfrak{z} = \frac{8}{\int_{\lambda_1}^{\lambda_2} q_{p,\lambda}^0 dt} \frac{dN/dt}{dt} \quad (1)$$

where 8 represents the number of electrons involved in the conversion of CO<sub>2</sub> to CH<sub>4</sub>;  $dN/dt$  represents the CH<sub>4</sub> evolution rate; and  $q_{p,\lambda}^0$  is the incident photon flux within a defined wavelength range (eg. 250 – 400 nm). The superscript 0 (zero) indicates that the incident number of

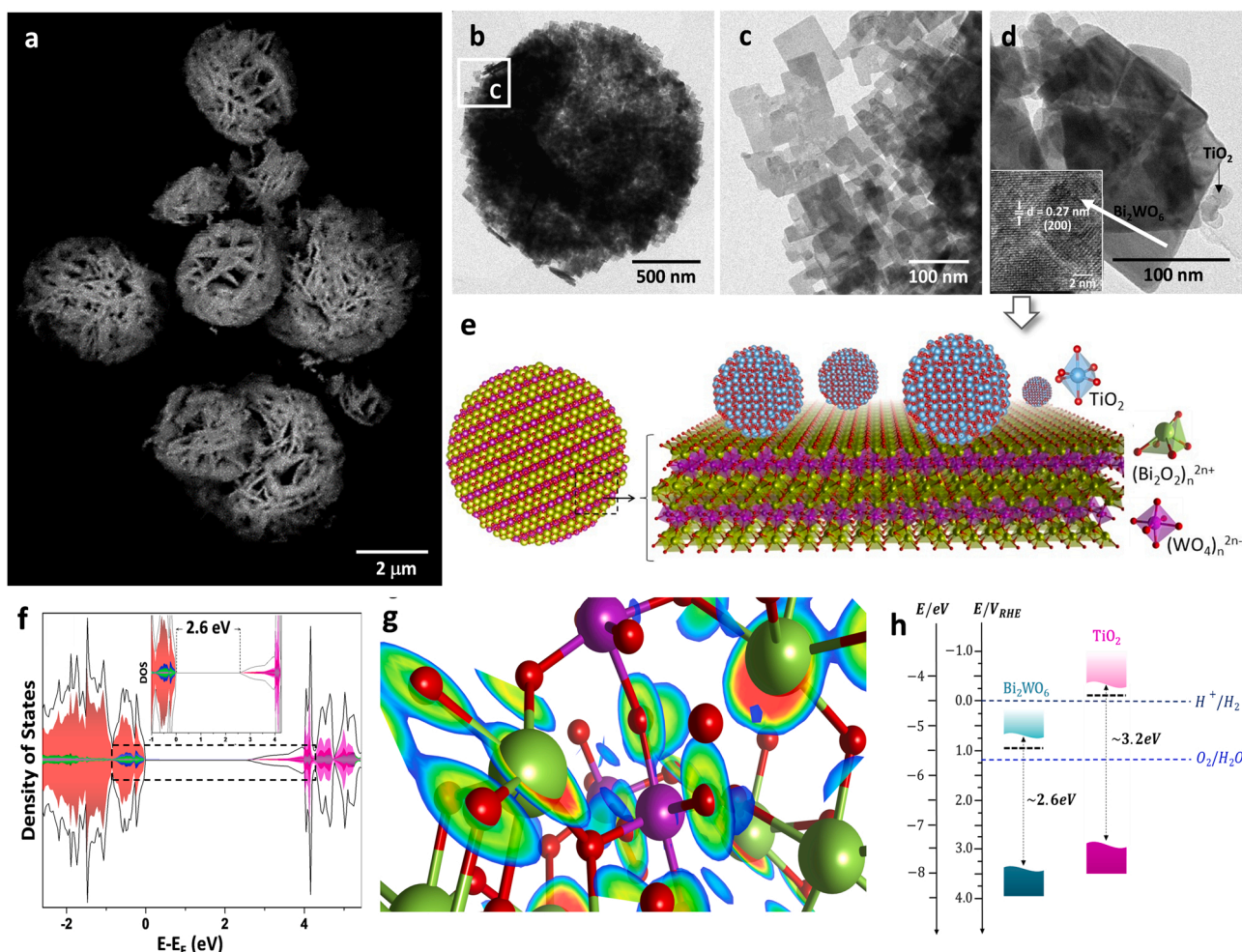


**Fig. 1.** (a) SEM image of BiW. TEM images of (b-c) BiW and (d) BiW/Ti17. (e) Schematic representation of the crystal structure and metal coordination of Bi<sub>2</sub>WO<sub>6</sub> and TiO<sub>2</sub> in BiW/Ti hybrids. (f) Density of states (DOS) and (g) electron localization function (ELF) plot for Bi<sub>2</sub>WO<sub>6</sub>. DOS colors: O 2p (red); Bi 5p (green), Bi 5s (blue), W 5d (magenta). Atom colors: O (red); Bi (green), W (magenta). (h) Band energy diagram of the Bi<sub>2</sub>WO<sub>6</sub> and anatase TiO<sub>2</sub>. Fermi level extracted from photoelectrochemical measurements and previous studies [3] for Bi<sub>2</sub>WO<sub>6</sub> and TiO<sub>2</sub>, respectively; Distance from fermi level to VBM calculated from XPS; band gap energy extracted from Tauc plot.



photons (prior to absorption) is also considered. The incident photon flux was calculated from the emission spectra of the UV lamps (see Fig. S1), which was recorded with a StellarNet UVNb-50 radiometer connected to an optical fiber.

### 3. Results and discussion

SEM analysis shows that the BiW sample consists on well-dispersed flower-like microspheres [18] with average diameters of 2 – 4  $\mu\text{m}$  (Fig. 1a). Each individual microsphere is composed of numerous rectangular nanoplates that confer a macroporous aspect to the structure. TEM analysis further corroborates the formation of rectangular nanoplates with side lengths of about 60 – 100 nm and widths of 30 – 60 nm, gathered on 2  $\mu\text{m}$  diameter microspheres (Fig. 1b-c). FESEM images and EDX elemental mapping (Fig. S2) revealed a close surface proximity of  $\text{Bi}_2\text{WO}_6$  and  $\text{TiO}_2$  in BiW/Ti heterostructures. TEM images (Fig. 1d-e) further showed the coexistence of both semiconductors and confirmed previous SEM observations, in which BiW/Ti samples are composed of  $\text{Bi}_2\text{WO}_6$  nanoplates and  $\text{TiO}_2$  nanoparticles between 5 and 23 nm average diameters.

Structural characterization by X-ray powder diffraction (Fig. S3a) shows that all diffraction peaks of bare BiW can be indexed to an orthorhombic well-crystallized  $\text{Bi}_2\text{WO}_6$  phase with lattice parameters  $a = 5.457 \text{ \AA}$ ,  $b = 5.436 \text{ \AA}$  and  $c = 16.427 \text{ \AA}$  (ICCD No. 73-1126, Pca2<sub>1</sub> space group). Its structure consists on perovskite-like  $(\text{WO}_4)_n^{2-}$  layers composed by  $\text{WO}_6$  octahedra layers separated by two  $(\text{Bi}_2\text{O}_2)_n^{2+}$  layers of corner-sharing  $\text{BiO}_x$  heptahedra [19] (Figs. 1e and S4). The crystal size is ca. 12 nm, based on the Scherrer equation. It was found that the intensity ratio of the (113) peak to the (200) peak in the sample is approximately 1.5 times higher than that of the russelite pattern, suggesting that the crystal has special anisotropic growth in (200) direction [20,21]. The lattice spacing of (200) plane is consistent with the interplanar distances of 0.27 nm measured from TEM images (Fig. 1d, inset) [20]. For BiW/Ti samples, both the typical diffraction peaks of  $\text{Bi}_2\text{WO}_6$  and the anatase phase of  $\text{TiO}_2$  (ICDD No. 21-1272, I41/amd space group) are observed in the composites (Fig. S3a). Besides, the position and shape of  $\text{Bi}_2\text{WO}_6$  peaks do not change in BiW/Ti samples, indicating that the incorporation of  $\text{TiO}_2$  in the heterojunction did not alter the lattice structure of  $\text{Bi}_2\text{WO}_6$ .

The Raman spectra (Fig. S3b) also allowed to distinguish bands corresponding to  $\text{Bi}_2\text{WO}_6$  and  $\text{TiO}_2$  within the BiW/Ti heterostructures. The characteristic bands of  $\text{TiO}_2$  anatase appear at 147 ( $E_g$ ), 394 ( $B_1g$ ), 515 ( $A_1g + B_1g$ ) and 637 ( $E_g$ )  $\text{cm}^{-1}$  [22]. The rest of the bands in the range 200–1000  $\text{cm}^{-1}$  are assigned to Raman active modes for Aurivillius  $\text{Bi}_2\text{WO}_6$  ( $2A_1 + B_1 + 3E_g$ ) [23]. In particular, the bands located at 791 and 825  $\text{cm}^{-1}$  are associated with the antisymmetric and symmetric stretching modes in  $\text{WO}_6$  octahedra, involving motions of the apical oxygen atoms [24,25]. The small band located at 709  $\text{cm}^{-1}$  is related to W-O stretching modes of equatorial oxygens within  $\text{WO}_6$  octahedra. Finally, the bands in the 240–350  $\text{cm}^{-1}$  region can be assigned to the bending vibration of  $\text{WO}_6$  and stretching and bending vibration of  $\text{BiO}_6$  polyhedra [23,26]. BiW/Ti samples exhibit the main Raman signals of both  $\text{Bi}_2\text{WO}_6$  and  $\text{TiO}_2$ -anatase, as expected for a hybrid heterojunction. Besides, the BiW/Ti50 heterojunction shows a slight shift towards higher wavenumbers in the bands associated with the antisymmetric stretching mode in  $\text{WO}_6$  octahedra (ca. 793  $\text{cm}^{-1}$ ) and the bending vibration of  $\text{WO}_6$  and  $\text{BiO}_6$  polyhedra (ca. 308  $\text{cm}^{-1}$ ), as compared to pure  $\text{Bi}_2\text{WO}_6$  (ca. 791 and 305  $\text{cm}^{-1}$ , respectively) (Fig. S3b), thus suggesting a strong interaction between  $\text{Bi}_2\text{WO}_6$  and  $\text{TiO}_2$  in BiW/Ti hybrids.

Regarding the textural properties, BiW sample exhibits a typical type II isotherm with a H3-type hysteresis loop (Fig. S5) [27]. Such kind of hysteresis loop is associated with aggregates of plate-like particles [28], in good agreement with the hierarchical morphology observed in SEM and TEM images (Fig. 1a-c). The Brunauer–Emmett–Teller (BET) surface area calculated from the  $\text{N}_2$  adsorption–desorption isotherms was 20  $\text{m}^2 \text{g}^{-1}$ . As expected, increasing the  $\text{TiO}_2$  content in BiW/Ti samples led to

higher surface areas ranging from 18 to 88  $\text{m}^2 \text{g}^{-1}$  upon increasing the content of  $\text{TiO}_2$  (Table S1).

The optical absorption properties of the samples were analyzed by DRS UV–vis spectroscopy. BiW presents an intense absorption band from the UV light region to visible wavelengths shorter than 450 nm (Fig. S6a), which is consistent with the yellowish color of the powdered catalyst. The band gap of the photocatalyst is estimated to be 2.65 eV from the onset of the absorption edge (Fig. S6b), in good agreement with theoretical calculations (Fig. 1f). The steep shape of the DRS UV–vis spectra indicates that the visible light absorption arises from the electronic transition in  $\text{Bi}_2\text{WO}_6$  rather than from impurity levels [29]. In the case of BiW/Ti hybrids, increasing ratios of  $\text{Bi}_2\text{WO}_6$  led to a slightly red-shifted absorption edge within the visible-light range, thus extending the spectral response of the hybrids.

Regarding the electronic structure of  $\text{Bi}_2\text{WO}_6$ , the total density of states (DOS) (Fig. 1f) shows that the valence band maximum (VBM) is composed by O 2p states hybridized with Bi 6s 6p orbitals, while the conduction band minimum (CBM) is mainly formed by O 2p and W 5d orbitals, both separated by an estimated band gap of 2.6 eV. Electron localization function (ELF) plot (Fig. 1g) shows a predominant charge distribution in Bi and O atoms, confirming the formation of hybridized orbitals.

Fig. S7 shows plots of the photoelectron spectrum of  $\text{Bi}_2\text{WO}_6$  in the Bi 4f, W 4f, O 1s, and valence band regions. The Bi 4f and W 4f regions have peak of intensity at 159.7 eV and 36.0 eV, respectively, which are expected values for  $\text{Bi}^{3+}$  and  $\text{W}^{6+}$  cation in  $\text{Bi}_2\text{WO}_6$  [30]. The spectrum in the VB region has an onset at 2.6 eV, which coincides with theoretical and experimental estimations of the band gap of this material (see UV–visible spectroscopy study in Fig. S6). Provided all photoelectron emission spectra are referenced to the Fermi level (i.e., the Fermi level is set as 0 eV), this indicates that the Fermi level ( $E_F$ ) in the synthesized material is close to the CBM, and therefore behaves as an n-type semiconductor.

#### 3.1. Photocatalytic performance of BiW/Ti hybrids for the $\text{CO}_2$ reduction

The gas-phase  $\text{CO}_2$  photoreduction performance of BiW and BiW/Ti hybrids was investigated under UV illumination to induce the excitation of both semiconductors. BiW is mainly active in the formation of CO and  $\text{H}_2$ , together with minor amounts of  $\text{CH}_4$  and  $\text{C}_2\text{H}_4\text{O}_2$  (Table S2). On the other hand, coupling  $\text{Bi}_2\text{WO}_6$  and  $\text{TiO}_2$  semiconductors in BiW/Ti hybrids led to a 39.8- and 2.7-fold increase in  $\text{CH}_4$  production (Fig. 2a and Table S2), compared to that of bare BiW and  $\text{TiO}_2$ , respectively. BiW/Ti catalysts also yield  $\text{H}_2$  and CO, as well as minor amounts of  $\text{C}_2\text{H}_4\text{O}_2$ ,  $\text{C}_2\text{H}_4$  and  $\text{C}_2\text{H}_6$  (Table S2). The highest  $\text{CH}_4$  production is obtained with BiW/Ti50, reaching a value of 15.9  $\mu\text{mol g}_{\text{cat}}^{-1}$  after 15 h of UV illumination, which is higher than that obtained with both single materials (Fig. 2b). The selectivity of the hybrids clearly changed towards the formation of more electron-demanding products such as  $\text{CH}_4$  and  $\text{C}_2+$  products. Namely,  $\text{H}_2$  productions decreased by half and accordingly, the selectivity towards  $\text{CH}_4$  increased by 5 to 6-times in BiW/Ti hybrids compared to BiW (Table S2).

Interestingly, the  $\text{CH}_4$  production of BiW/Ti50 reaches or even surpasses the state-of-the-art literature [16,31,32] with  $\text{Bi}_2\text{WO}_6/\text{TiO}_2$ , but here using a significantly lower density of power illumination (ca. 19.1-times less UV power) [32]. Besides, this material presents a photonic efficiency towards  $\text{CH}_4$  of 0.028%, which is 28-times higher than that of BiW (Fig. 2a).

A study of  $\text{CO}_2/\text{H}_2\text{O}$  interaction with different catalysts on near-ambient pressure XPS (NAP-XPS) suggests that  $\text{CO}_2$  adsorption is preferable over  $\text{TiO}_2$  active sites. Fig. S8a shows the XPS of  $\text{Bi}_2\text{WO}_6$  in the C 1s region under a  $\text{CO}_2/\text{H}_2\text{O}$  environment. Contributions from aliphatic C and C-O species (284.6 eV and 286.5 eV, respectively) can be fitted in the spectrum; however, the region of C=O associated with carbonate/bicarbonate species [33] is completely flat. On the other hand, as shown in Fig. S8b, an additional contribution associated with C=O species

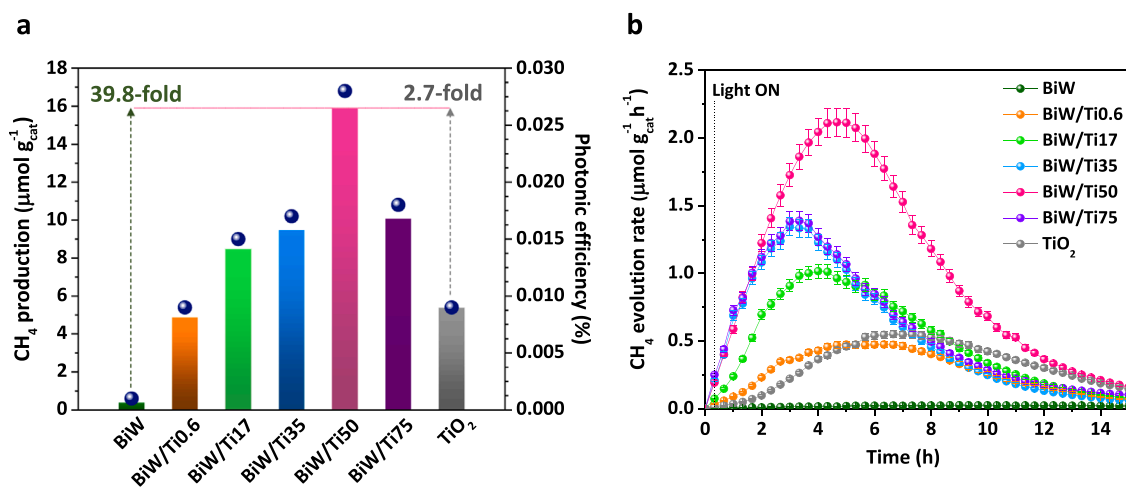


**Fig. 2.** Gas-phase photocatalytic CO<sub>2</sub> reduction towards CH<sub>4</sub> over BiW, BiW/Ti hybrids and bare TiO<sub>2</sub>. (a) Cumulative production (bars) and photonic efficiencies (dots) after 15 h of UV illumination. (b) CH<sub>4</sub> evolution rates.

(289.5 eV) can be fitted in the C 1 s spectrum of BiW/Ti50 under the same CO<sub>2</sub>/H<sub>2</sub>O environment. In this case, the concentration of C=O species is 5%. Such increase of oxygenated species on the catalyst

surface of BiW/Ti is associated with the unavoidable presence of adsorbed carbonates [33]. For comparison purpose, Fig. S8c shows the XPS of TiO<sub>2</sub> in the C 1 s region under the same CO<sub>2</sub>/H<sub>2</sub>O environment.

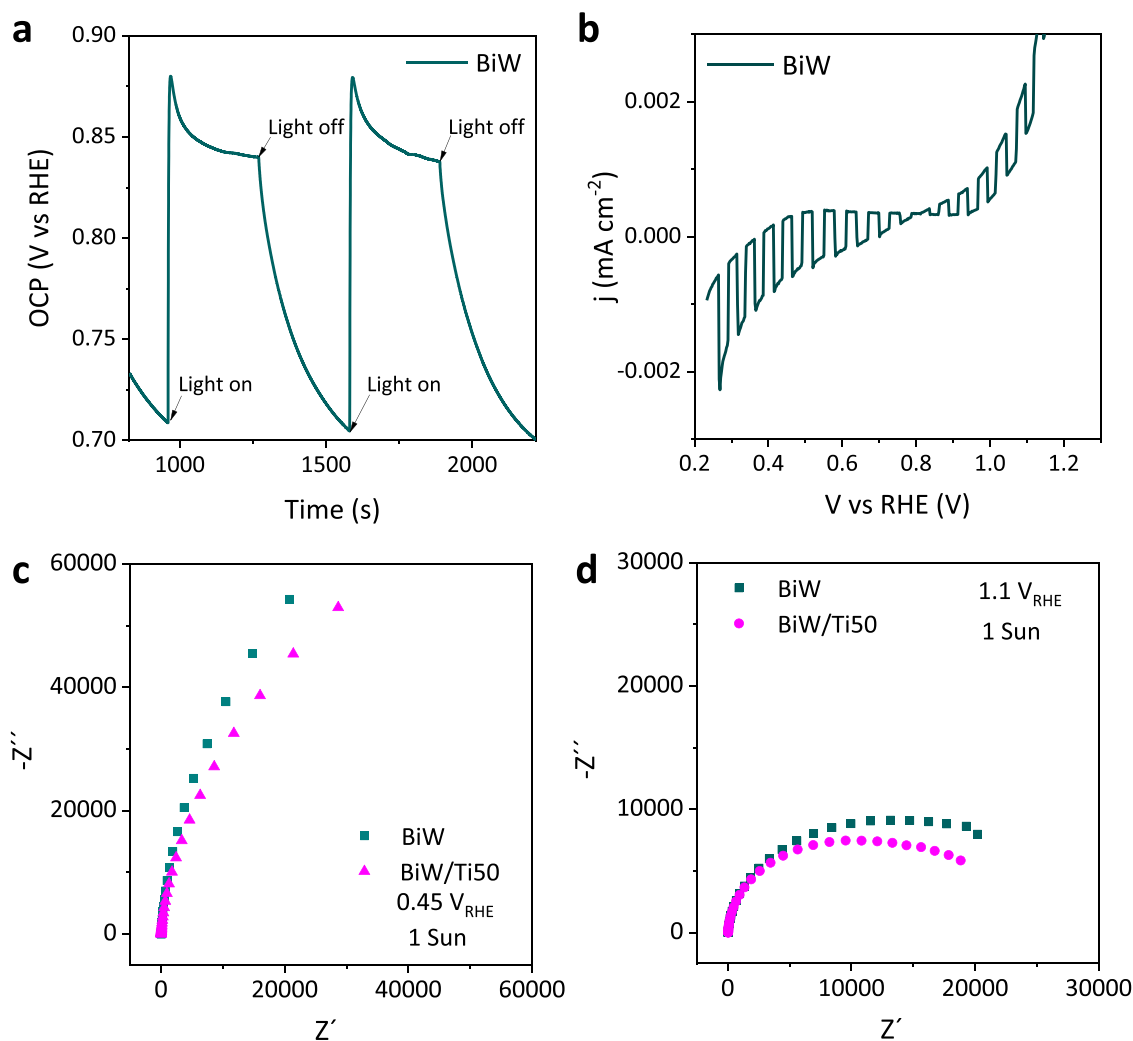


**Fig. 3.** (a) Open Circuit Potential (OCP) under dark and under illumination and (b) Linear sweep voltammetry under chopped illumination for BiW sample. Comparison between the Nyquist plots acquired in the BiW and BiW/Ti50 samples under illumination at (c) the cathodic region at 0.45 V vs RHE and (d) the anodic region at 1.1 V vs RHE.

As expected, the spectrum can be fitted with strong contributions from C=O (289.7 eV) with concentrations of 11%. These results indicate that the adsorption of CO<sub>2</sub> preferentially occurs on TiO<sub>2</sub> as carbonate/bicarbonate species, that participate in both reaction and deactivation pathways [33,34]. This fact can be associated to the decrease in the methane production for higher TiO<sub>2</sub> concentrations.

### 3.2. Photocarrier characterization

Fig. 3a shows the open circuit potential (OCP) of the Bi<sub>2</sub>WO<sub>6</sub> under chopped illumination, revealing a photocathodic behavior, since the OCP increases under illumination. On the other hand, Fig. 3b shows the aspect of a linear sweep voltammetry under chopped illumination of BiW. As it can be observed, the sample shows a photo-responsive behavior in both cathodic and anodic directions with an experimental value of the flat band potential ( $V_{FB}$ ) around 0.82 V vs RHE. Although an n-type semiconductor like Bi<sub>2</sub>WO<sub>6</sub> is expected to behave as a photoanode (like TiO<sub>2</sub> or BiVO<sub>4</sub>), such positive  $V_{FB}$  value is more typical in well-known photocathode materials like CuO and Cu<sub>2</sub>O, which may result in the observed dual photoelectrocatalytic behavior that has indeed been recently reported for Bi<sub>2</sub>WO<sub>6</sub> photoelectrodes [35]. This fact also indicates that the bands energy position in Bi<sub>2</sub>WO<sub>6</sub> are deeper than those of TiO<sub>2</sub>, and also deeper than the redox potential of hydrogen production from water splitting (i.e.  $E^0(H^+/H_2) = 0 V_{RHE}$ ), as depicted in Fig. 1h.

Moreover, Electrochemical Impedance Spectroscopy (EIS) measurements were performed to gain mechanistic insights regarding the charge transfer processes. Fig. 3c and d show the comparison between the Nyquist plots corresponding to BiW and BiW/Ti50 samples under illumination at 0.45 and 1.1 V vs RHE, respectively. In both regions, the hybrid BiW/Ti50 sample shows a lower resistance than the BiW reference, as it can be observed in Fig. S9, which is a direct indication of an enhanced charge transfer process in the hybrid compound compared with bare BiW reference.

Further, it is well-known that there is a strong correlation between photophysical properties and photocatalytic performance. Therefore, we carried out a combined study of photoluminescence (PL), time-resolved photoluminescence (TR PL) and transient absorption spectroscopy (TAS) to study the recombination of photogenerated charges in all prepared materials.

Fig. S10a shows a significantly lower PL intensity of all BiW/Ti hybrids compared to pure BiW or TiO<sub>2</sub> (Fig. S10a, green and grey traces, respectively); however, since both materials absorb in the UV range, it is difficult to discern if the reduction originates from the heterojunction or from a filter effect contribution. To avoid this effect, TR PL was performed upon UV illumination ( $\lambda_{exc} = 372$  nm, band-pass of 450 nm), showing a progressive reduction in the lifetime ( $\tau_F$ ) in the first 1–2 ns upon increasing the TiO<sub>2</sub> content. This was accompanied with an enhance in the signal after 2 ns, which showed an isosbestic point as a consequence of the synergetic effect of the hybrids. This finding suggests a more efficient suppression of radiative recombination of photo-excited electrons and holes within the heterostructures [16]. From 2 ns, the signal approaches to TiO<sub>2</sub> control (Fig. S10b). Clearly, the signals observed in the hybrids do not correspond to the sum of the contributions of the bare materials. The greatest effect was observed for the hybrid BiW/Ti50. According to the diagram of CB/VB bands (Fig. 1h), an interfacial charge transfer could occur from Bi<sub>2</sub>WO<sub>6</sub> to TiO<sub>2</sub>, mostly in timescales faster than a few nanoseconds.

After photon absorption, the generation and trapping of photo-generated charges in semiconductors occur in the fs to ps timescale [36, 37]. However, recombination and dynamic charge transfer events can be monitored by nanosecond-microsecond transient absorption spectroscopy (TAS) [38,39].

For Bi<sub>2</sub>WO<sub>6</sub> semiconductor, no specific references of TAS measurements were found in the ns -  $\mu$ s timescale. For this reason, we first studied the photophysical behavior of the benchmark TiO<sub>2</sub> and

compared it with the Bi<sub>2</sub>WO<sub>6</sub> semiconductor (Supplementary Materials, section **Transient Absorption Spectroscopy studies and Figs. S11 and S12**). In order to identify the transient absorption bands and its corresponding kinetics, TiO<sub>2</sub> and Bi<sub>2</sub>WO<sub>6</sub> aqueous suspension solutions were measured in the absence or presence of acceptor-donor scavengers. Specifically, an aqueous solution of potassium persulfate K<sub>2</sub>S<sub>2</sub>O<sub>8</sub> 10 mM or 1 wt% Pt were used as electron acceptors for the identification of the photoholes signal, while methanol (10% v/v) was employed as hole scavenger.

From this study we conclude that at low laser pulse energies (300  $\mu$ J), both electron and hole species coexist with different percentage contribution; whereas mainly photogenerated electrons can be observed at higher energies (2 mJ). Furthermore, bare Bi<sub>2</sub>WO<sub>6</sub> exhibited short-lived carriers ( $\tau = 25$  ns,  $\lambda_{exc} = 355$  nm, 2 mJ/pulse) than pristine TiO<sub>2</sub> ( $\tau = 50$  ns), in consistency with the higher photocatalytic H<sub>2</sub> production of TiO<sub>2</sub>. This highlights the need to improve the photocatalytic properties of Bi<sub>2</sub>WO<sub>6</sub> by combination with titania in the hybrid materials.

TAS measurements for hybrids and their corresponding bare materials were performed to gain insights into the charge transfer mechanism. Several examples have been reported in literature, which show that the hybrid structure facilitates the efficient dissociation of charge carriers at the interface of the photocatalyst [40–42]. Following the exciton ( $e^-/h^+$  pair) formation upon illumination, electrons and holes can be easily transferred to electron and hole acceptors, respectively, as previously demonstrated herein. The quantum efficiency of these processes competes with the charge-transfer rate at the interface of the hybrids, and with the intrinsic recombination rate within the particles.

To clearly monitor the electron transfer process in the hybrids, TAS measurements were carried out with MeOH (10% v/v) and a laser pulse energy of 2 mJ to favor a greater generation of photoelectrons and to avoid the mixture of hole + electron TAS signal observed at low energy excitation (Figs. S10 and S11). The transient absorption spectral profile of the most active hybrid (BiW/Ti50) shows a higher contribution of electrons in visible range than Bi<sub>2</sub>WO<sub>6</sub> (Fig. 4a), consistently with the enhanced photocatalytic efficiency of the hybrids compared with that of the bare semiconductor. This signal is higher than the corresponding theoretical signal considering a 50% wt/wt of each semiconductor (Fig. 4a).

Next, the temporal profiles for the four hybrids and bare semiconductors were compared upon excitation at 460 nm (Fig. 4b). The hybrids show a remarkable enhancement of the lifetimes at  $\lambda_{mon} = 460$  nm compared to that of Bi<sub>2</sub>WO<sub>6</sub>, confirming a lower electron-hole recombination process. Increasing the amount of TiO<sub>2</sub> in the hybrids was expected to lead to a more significant spectral overlap and stronger coupling between the donor and acceptor states, thus resulting in a faster electron transfer. Electron–phonon relaxation for both Bi<sub>2</sub>WO<sub>6</sub> and TiO<sub>2</sub> competes with the electron transfer process in the hybrids and results in an electronic energy loss. In the hybrids, the electrons and holes in TiO<sub>2</sub> decay within the bandgap to the edges of the corresponding conduction and valence bands, and survive for longer lifetimes promoting the interaction with the Bi<sub>2</sub>WO<sub>6</sub> counterpart at the interface, thus leading to a higher oxidative and reductive power of the hybrids.

Decays in Fig. 4b show two differentiated regions that explain the observed enhancement in the hybrids' lifetime. First, a short timescale up to 20 ns where no changes were detected with the controls, and which probably corresponds to the tail of the photogenerated electrons after the laser pulse (usually in the femtosecond scale). Secondly, a higher lifetimes region around 20–500 ns, in which there is an increase in the hybrids' signals as a result of the migration and delocalization of the electrons, leading to higher charge separation efficiencies. In this second region, BiW/Ti50 exhibits the longest lifetime (Fig. 4b) in good agreement with the greater photocatalytic activity for this hybrid compared to the bare Bi<sub>2</sub>WO<sub>6</sub> semiconductor. This behavior agrees with the improved performance of other TiO<sub>2</sub>-based hybrids [43] due to their longer carriers lifetime. Finally, no changes were observed at a longer

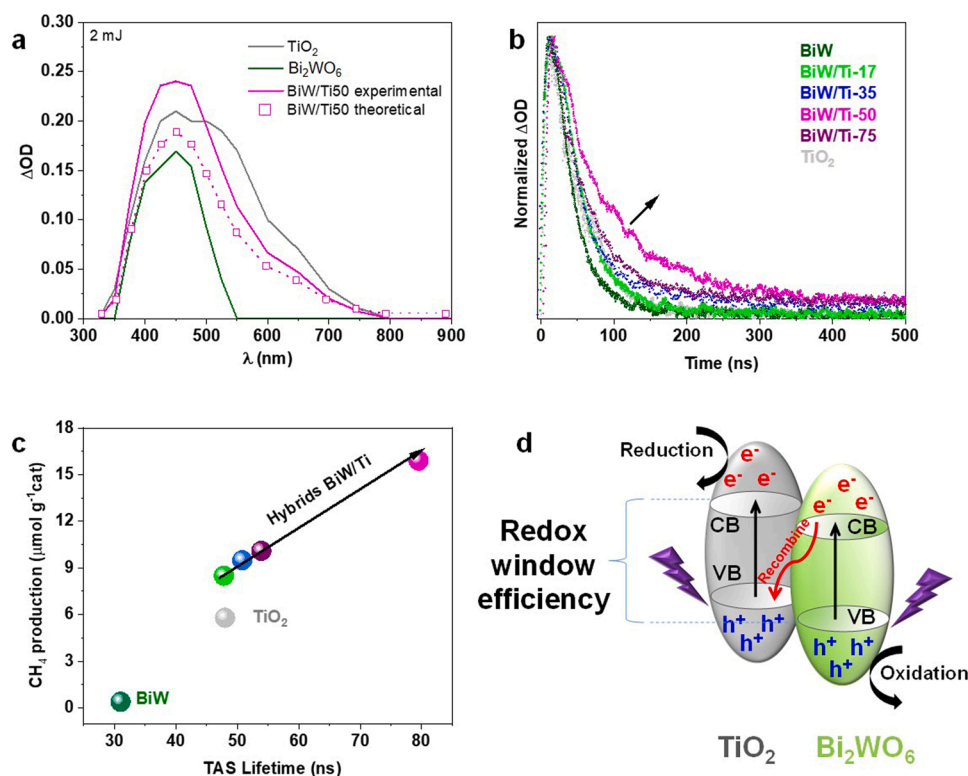


**Fig. 4.** (a) Transient absorption spectra ( $\lambda_{\text{exc}} = 355$  nm) for  $\text{Bi}_2\text{WO}_6$  (red),  $\text{TiO}_2$  (grey) and the hybrid  $\text{BiW}/\text{Ti}50$  (blue) under deaerated aqueous suspension solutions containing MeOH (10% v/v). Theoretical TA spectra (pink squares) is included for comparison. (b) Normalized transient decays ( $\lambda_{\text{exc}} = 355$  nm,  $\lambda_{\text{mon}} = 460$  nm) for  $\text{Bi}_2\text{WO}_6$  (red),  $\text{TiO}_2$  (grey) and the hybrids in deaerated aqueous methanol 10 vol% suspensions. (c) Relationship between  $\text{CO}_2$  photoreduction reaction vs transient lifetime for the bare  $\text{Bi}_2\text{WO}_6$  and hybrids heterojunctions with  $\text{TiO}_2$ . (d) Charge transfer mechanism in  $\text{Bi}_2\text{WO}_6/\text{TiO}_2$  heterojunctions.

microsecond timescale. These findings, combined with the calculated redox potentials (Fig. 1h), clearly indicate that the electron population in  $\text{TiO}_2$  occurs from  $\text{Bi}_2\text{WO}_6$  following the electron transfer mechanism showed in Fig. 4d. These results are consistent with the reported literature for  $\text{BiW}/\text{Ti}$  systems or hybrids containing  $\text{BiW}$  [44–49], although it had not been demonstrated by TAS until now. A direct relationship between the transients of the hybrids and their  $\text{CO}_2$  photoreduction performance was observed by plotting lifetimes against photoactivity (Fig. 4c). The transient signal of  $\text{BiW}/\text{Ti}50$  surpasses that of  $\text{Bi}_2\text{WO}_6$  or  $\text{TiO}_2$ , confirming the synergistic effect between the two inorganic semiconductors within the heterojunction.

#### 4. Conclusions

A bismuth-tungsten mixed oxide and a series of  $\text{Bi}_2\text{WO}_6/\text{TiO}_2$  heterojunctions were prepared following hydrothermal methods. All materials are photocatalytically active towards the  $\text{CO}_2$  reduction with water as reductant agent, although hybrid heterojunctions show considerably improved performances. Interestingly,  $\text{CO}_2$  photoreduction tests clearly show a selectivity change for the hybrids towards the formation of more electron-demanding products. Among them,  $\text{BiW}/\text{Ti}50$  exhibits the highest  $\text{CH}_4$  production, surpassing that obtained with single  $\text{Bi}_2\text{WO}_6$  and  $\text{TiO}_2$ . The superior photoactivity of  $\text{BiW}/\text{Ti}$  hybrids compared to bare  $\text{Bi}_2\text{WO}_6$  is ascribed to the more efficient charge transfer mechanism in the heterojunction. Photoelectrochemical measurements demonstrate an enhanced charge transfer in hybrids, showing a decrease in the charge transfer resistance upon illumination. Besides, charge dynamics studies reveal a prolonged lifetime of photogenerated carriers in hybrids and retarded recombination rates due to the enhanced charge transfer mechanism in the heterojunction. In addition, NAP-XPS studies show a preferential adsorption of  $\text{CO}_2$  as carbonate/bicarbonate species over  $\text{TiO}_2$  active sites, which participate in both reaction and deactivation pathways. These findings seem to indicate that the improvement in the photoactivity of the hybrids is due to an enhanced charge transfer that contributes to the creation of spatially separated photocatalytic sites, in which reduction and oxidation occur

on  $\text{TiO}_2$  and  $\text{Bi}_2\text{WO}_6$ , respectively.

#### CRediT authorship contribution statement

**Laura Collado:** Conceptualization, Methodology, Investigation, Writing – original draft, Visualization. **Miguel Gomez-Mendoza:** Methodology, Investigation, Writing – original draft. **Miguel García-Tecedor:** Methodology, Investigation, Writing – original draft. **Freddy E. Oropeza:** Methodology, Investigation. **Anna Reynal:** Conceptualization, Validation. **James R. Durrant:** Conceptualization, Validation. **David P. Serrano:** Conceptualization, Supervision. **Víctor A. de la Peña O'Shea:** Conceptualization, Validation, Supervision, Project administration, Funding acquisition.

#### Declaration of Competing Interest

The authors declare that they have no known competing financial interests or personal relationships that could have appeared to influence the work reported in this paper.

#### Data availability

No data was used for the research described in the article.

#### Acknowledgments

Financial support has been received from the European Research Council (ERC), through HYMAP project (grant agreement No. 648319), under the European Union's Horizon 2020 research and innovation program, as well as from the Marie Skłodowska-Curie grant agreement No. 754382. L.C. acknowledges funding from the project ARMONIA (PID2020-119125RJ-I00) funded by MCIN/AEI/10.13039/501100011033. Financial support has also been received from AEI-MINECO/FEDER (Nympha Project, PID2019-106315RB-I00), "Comunidad de Madrid" regional government, and the European Structural Funds (FotoArt-CM project, S2018/NMT-4367). Authors also



acknowledge financial support from the grant PLEC2021–007906 funded by MCIN/AEI/10.13039/501100011033 and the “European Union NextGenerationEU/PRTR”.

### Declaration of Competing Interest

The authors declare no known competing financial interests or personal relationships that could influence the reported work in this paper.

### Appendix A. Supporting information

Supplementary data associated with this article can be found in the online version at [doi:10.1016/j.apcatb.2022.122206](https://doi.org/10.1016/j.apcatb.2022.122206).

### References

- [1] R.C. Armstrong, C. Wolfram, K.P. De Jong, R. Gross, N.S. Lewis, B. Boardman, A. J. Ragauskas, K. Ehrhardt-Martinez, G. Crabtree, M.V. Ramana, The frontiers of energy, *Nat. Energy* 1 (2016) 1–8, <https://doi.org/10.1038/nenergy.2015.20>.
- [2] S. Chu, A. Majumdar, Opportunities and challenges for a sustainable energy future, *Nature* 488 (2012) 294–303, <https://doi.org/10.1038/nature11475>.
- [3] L. Collado, A. Reynal, F. Fresno, M. Barawi, C. Escudero, V. Perez-dieste, J. M. Coronado, D.P. Serrano, J.R. Durrant, V.A. de la Peña O'Shea, Unravelling the effect of charge dynamics at the plasmonic metal/semiconductor interface for CO<sub>2</sub> photoreduction, *Nat. Commun.* 9, Art. 4986 (Number) (2018) 1–10, <https://doi.org/10.1038/s41467-018-07397-2>.
- [4] I.D. Young, M. Ibrahim, R. Chatterjee, S. Gul, F.D. Fuller, S. Koroidov, A. S. Brewster, R. Tran, R. Alonso-Mori, T. Kroll, T. Michels-Clark, H. Laksmono, R. G. Sierra, C.A. Stan, R. Hussein, M. Zhang, L. Douthit, M. Kubin, C. de Lichtenberg, L.V. Pham, H. Nilsson, M.H. Cheah, D. Shevela, C. Saracini, M.A. Bean, I. Seuffert, D. Sokaras, T.-C. Weng, E. Pastor, C. Weninger, T. Fransson, L. Lassalle, P. Bräuer, P. Aller, P.T. Docker, B. Andi, A.M. Orville, J.M. Glowina, S. Nelson, M. Sikorski, D. Zhu, M.S. Hunter, T.J. Lane, A. Aquila, J.E. Koglin, J. Robinson, M. Liang, S. Boutet, A.Y. Lyubimov, M. Uevirojjangkoorn, N.W. Moriarty, D. Liebschner, P. V. Afonine, D.G. Waterman, G. Evans, P. Wernet, H. Dobbek, W.I. Weis, A. T. Brunger, P.H. Zwart, P.D. Adams, A. Zouni, J. Messinger, U. Bergmann, N. K. Sauter, J. Kern, V.K. Yachandra, J. Yano, Structure of photosystem II and substrate binding at room temperature, *Nature* 540 (2016) 453–457, <https://doi.org/10.1038/nature20161>.
- [5] N. Li, X.P. Zhai, W.K. Yan, Y.J. Zhang, Z.T. Zhang, M.J. Xiao, X.D. Zhang, Q. Wang, H.L. Zhang, Boosting cascade electron transfer for highly efficient CO<sub>2</sub> photoreduction, *Sol. Rrl.* 5 (2021) 2100558, <https://doi.org/10.1002/solr.202100558>.
- [6] L. Collado, A. Reynal, J.M. Coronado, D.P. Serrano, J.R. Durrant, V.A. de la Peña O'Shea, Effect of Au surface plasmon nanoparticles on the selective CO<sub>2</sub> photoreduction to CH<sub>4</sub>, *Appl. Catal. B Environ.* 178 (2015) 177–185, <https://doi.org/10.1016/j.apcatb.2014.09.032>.
- [7] M. Barawi, L. Collado, M. Gomez-Mendoza, F.E. Oropeza, M. Liras, V.A. de la Peña, O'Shea, Conjugated Porous Polymers: Ground-Breaking Materials for Solar Energy Conversion, *Adv. Energy Mater.* 2101530 (2021) 1–31, <https://doi.org/10.1002/aenm.202101530>.
- [8] S. Murcia-López, M.C. Hidalgo, J.A. Navío, Photocatalytic activity of single and mixed nanosheet-like Bi<sub>2</sub>WO<sub>6</sub> and TiO<sub>2</sub> for Rhodamine B degradation under sunlike and visible illumination, *Appl. Catal. A Gen.* 423–424 (2012) 34–41, <https://doi.org/10.1016/j.apcata.2012.02.016>.
- [9] G. Colón, S. Murcia López, M.C. Hidalgo, J.A. Navío, Sunlight highly photoactive Bi<sub>2</sub>WO<sub>6</sub>-TiO<sub>2</sub> heterostructures for rhodamine B degradation, 4809–11, *Chem. Commun. (Camb.)* 46 (2010), <https://doi.org/10.1039/c0cc00058b>.
- [10] Y. Liu, D. Shen, Q. Zhang, Y. Lin, F. Peng, Enhanced photocatalytic CO<sub>2</sub> reduction in H<sub>2</sub>O vapor by atomically thin Bi<sub>2</sub>WO<sub>6</sub> nanosheets with hydrophobic and nonpolar surface, *Appl. Catal. B Environ.* 283 (2021) 119630–119639, <https://doi.org/10.1016/j.apcatb.2020.119630>.
- [11] L. Zhang, W. Wang, L. Zhou, H. Xu, Bi<sub>2</sub>WO<sub>6</sub> Nano- and microstructures: Shape control and associated visible-light-driven photocatalytic activities, *Small* 3 (2007) 1618–1625, <https://doi.org/10.1002/sml.200700043>.
- [12] L. Zhang, H. Wang, Z. Chen, P.K. Wong, J. Liu, Bi<sub>2</sub>WO<sub>6</sub> micro/nano-structures: Synthesis, modifications and visible-light-driven photocatalytic applications, *Appl. Catal. B Environ.* 106 (2011) 1–13, <https://doi.org/10.1016/j.apcatb.2011.05.008>.
- [13] A. Kumar, P. Singh, A.A.P. Khan, Q. Van Le, V.H. Nguyen, S. Thakur, P. Raizada, CO<sub>2</sub> photoreduction into solar fuels via vacancy engineered bismuth-based photocatalysts: Selectivity and mechanistic insights, *Chem. Eng. J.* 439 (2022), 135563, <https://doi.org/10.1016/j.cej.2022.135563>.
- [14] S. Banerjee, S.C. Pillai, P. Falaras, K.E. O'Shea, J.A. Byrne, D.D. Dionysiou, New Insights into the Mechanism of Visible Light Photocatalysis, *J. Phys. Chem. Lett.* 5 (2014) 2543–2554, <https://doi.org/10.1021/jz501030x>.
- [15] J. Xu, W. Wang, S. Sun, L. Wang, Enhancing visible-light-induced photocatalytic activity by coupling with wide-band-gap semiconductor: A case study on Bi<sub>2</sub>WO<sub>6</sub>/TiO<sub>2</sub>, *Appl. Catal. B Environ.* 111–112 (2012) 126–132, <https://doi.org/10.1016/j.apcatb.2011.09.025>.
- [16] L. Yuan, K.Q. Lu, F. Zhang, X. Fu, Y.J. Xu, Unveiling the interplay between light-driven CO<sub>2</sub> photocatalytic reduction and carbonaceous residues decomposition: A case study of Bi<sub>2</sub>WO<sub>6</sub>-TiO<sub>2</sub> binanosheets, *Appl. Catal. B Environ.* 237 (2018) 424–431, <https://doi.org/10.1016/j.apcatb.2018.06.019>.
- [17] K. Li, C. Teng, S. Wang, Q. Min, Recent Advances in TiO<sub>2</sub>-Based Heterojunctions for Photocatalytic CO<sub>2</sub> Reduction With Water Oxidation: A Review, *Front. Chem.* 9 (2021) 1–25, <https://doi.org/10.3389/fchem.2021.637501>.
- [18] J. He, W. Wang, F. Long, Z. Zou, Z. Fu, Z. Xu, Hydrothermal synthesis of hierarchical rose-like Bi<sub>2</sub>WO<sub>6</sub> microspheres with high photocatalytic activities under visible-light irradiation, *Mater. Sci. Eng. B* 177 (2012) 967–974, <https://doi.org/10.1016/j.mseb.2012.04.018>.
- [19] J. Tian, Y. Sang, G. Yu, H. Jiang, X. Mu, H. Liu, A Bi<sub>2</sub>WO<sub>6</sub>-based hybrid photocatalyst with broad spectrum photocatalytic properties under UV, visible, and near-infrared irradiation, *Adv. Mater.* 25 (2013) 5075–5080, <https://doi.org/10.1002/adma.201302014>.
- [20] A. Phuruangrat, P. Dumrongrojthanath, N. Ekthammathat, S. Thongtem, T. Thongtem, Hydrothermal Synthesis, Characterization, and Visible Light-Driven Photocatalytic Properties of Bi<sub>2</sub>WO<sub>6</sub> Nanoplates, *J. Nanomater.* 2014 (2014) 1–7, <https://doi.org/10.1155/2014/138561>.
- [21] Z. Yang, L. Chen, Y. Yang, Construction of an all-solid-state artificial Z-scheme system consisting of Bi<sub>2</sub>WO<sub>6</sub>/Au/CdS nanostructure for photocatalytic CO<sub>2</sub> reduction into renewable hydrocarbon fuel, *Nanotechnology* 28 (2017) 2–10, <https://doi.org/10.1088/1361-6528/aa6bb5>.
- [22] P. Reñones, F. Fresno, J.L.G. Fierro, V.A. de la Peña O'Shea, Effect of La as Promoter in the Photoreduction of CO<sub>2</sub> Over TiO<sub>2</sub> Catalysts, *Top. Catal.* 60 (2017) 1119–1128, <https://doi.org/10.1007/s11244-017-0797-x>.
- [23] S. Obregón, G. Colón, Erbium doped TiO<sub>2</sub>-Bi<sub>2</sub>WO<sub>6</sub> heterostructure with improved photocatalytic activity under sun-like irradiation, *Appl. Catal. B Environ.* 140–141 (2013) 299–305, <https://doi.org/10.1016/j.apcatb.2013.04.014>.
- [24] M. Maczka, F. Fuentes, K. Hermanowicz, L. Macalik, P.E. Tomaszewski, L. Kępiński, R. Lisiecki, Luminescence and Phonon Properties of Nanocrystalline Bi<sub>2</sub>WO<sub>6</sub>: Eu<sup>3+</sup> Photocatalyst Prepared from Amorphous Precursor, *J. Nanosci. Nanotechnol.* 10 (2010) 5746–5754, <https://doi.org/10.1166/jnn.2010.2465>.
- [25] X.Y. Kong, Y.Y. Choo, S.P. Chai, A.K. Soh, A.R. Mohamed, Oxygen vacancy induced Bi<sub>2</sub>WO<sub>6</sub> for the realization of photocatalytic CO<sub>2</sub> reduction over the full solar spectrum: from the UV to the NIR region, *Chem. Commun.* 52 (2016) 14242–14245, <https://doi.org/10.1039/c6cc07750a>.
- [26] S. Murcia López, M.C. Hidalgo, J.A. Navío, G. Colón, Novel Bi<sub>2</sub>WO<sub>6</sub>-TiO<sub>2</sub> heterostructures for Rhodamine B degradation under sunlike irradiation, 1425–34, *J. Hazard. Mater.* 185 (2011), <https://doi.org/10.1016/j.jhazmat.2010.10.065>.
- [27] K.S.W. Sing, D.H. Everett, R.A.W. Haul, L. Moscou, R.A. Pierotti, J. Rouquerol, T. Siemieniowska, Reporting physisorption data for gas/solid systems with special reference to the determination of surface area and porosity, *Pure Appl. Chem.* 57 (1985) 603–619, <https://doi.org/10.1002/9783527610044.hetcat0065>.
- [28] Z. Sun, Z. Yang, H. Liu, H. Wang, Z. Wu, Visible-light CO<sub>2</sub> photocatalytic reduction performance of ball-flower-like Bi<sub>2</sub>WO<sub>6</sub> synthesized without organic precursor: Effect of post-calcination and water vapor, *Appl. Surf. Sci.* 315 (2014) 360–367, <https://doi.org/10.1016/j.apsusc.2014.07.153>.
- [29] H. Fu, C. Pan, W. Yao, Y. Zhu, Visible-light-induced degradation of rhodamine B by nanosized Bi<sub>2</sub>WO<sub>6</sub>, *J. Phys. Chem. B* 109 (2005) 22432–22439, <https://doi.org/10.1021/jp052995j>.
- [30] J.F. Moulder, Handbook of X-ray Photoelectron Spectroscopy: A Reference Book of Standard Spectra for Identification and Interpretation of XPS Data, Physical Electronics Division, Perkin-Elmer Corporation, 1992.
- [31] L. Ye, Y. Deng, L. Wang, H. Xie, F. Su, Bismuth-based photocatalysts for solar photocatalytic carbon dioxide conversion, *ChemSusChem* 12 (2019) 3671–3701, <https://doi.org/10.1002/cssc.201901196>.
- [32] S. Murcia-López, V. Vaiano, M.C. Hidalgo, J.A. Navío, D. Sannino, Photocatalytic reduction of CO<sub>2</sub> over platinumised Bi<sub>2</sub>WO<sub>6</sub>-based materials, *Photobiochem. Photobiol. Sci.* 14 (2015) 678–685, <https://doi.org/10.1039/C4PP00407H>.
- [33] L. Collado, P. Reñones, J. Fierro, F. Fresno, L. Garrido, V. Pérez-Dieste, C. Escudero, M.D. Hernández-Alonso, J.M. Coronado, D.P. Serrano, V.A. de la Peña O'Shea, The role of the surface acidic/basic centers and redox sites on TiO<sub>2</sub> in the photocatalytic CO<sub>2</sub> reduction, *Appl. Catal. B Environ.* 303 (2022) 120931–120942, <https://doi.org/10.1016/j.apcatb.2021.120931>.
- [34] N.M. Dimitrijevic, B.K. Vijayan, O.G. Poluektov, T. Rajh, K.A. Gray, H. He, P. Zapol, Role of water and carbonates in photocatalytic transformation of CO<sub>2</sub> to CH<sub>4</sub>, *J. Am. Chem. Soc.* 133 (2011) 3964–3971, <https://doi.org/10.1021/ja108791u>.
- [35] R. Ullah, M. Pei, J. Wu, Y. Tian, Z. Gu, Q. Zhang, C. Song, Y. Yang, M. Ahmad, J. Zeb, F. Qayyum, Y. Liu, X. An, L. Gu, X. Wang, J. Zhang, Bifunctional Photoelectrode Driven by Charged Domain Walls in Ferroelectric Bi<sub>2</sub>WO<sub>6</sub>, *ACS Appl. Energy Mater.* 3 (2020) 4149–4154, <https://doi.org/10.1021/acsaem.0c00503>.
- [36] J. Tang, J.R. Durrant, D.R. Klug, Mechanism of photocatalytic water splitting in TiO<sub>2</sub>: Reaction of water with photoholes, importance of charge carrier dynamics, and evidence for four-hole chemistry, *J. Am. Chem. Soc.* 130 (2008) 13885–13891, <https://doi.org/10.1021/ja8034637>.
- [37] A. García-Sánchez, M. Gomez-Mendoza, M. Barawi, I.J. Villar-García, M. Liras, F. Gándara, V.A. De La Peña O'Shea, Fundamental Insights into Photoelectrocatalytic Hydrogen Production with a Hole-Transport Bismuth Metal-Organic Framework, *J. Am. Chem. Soc.* 142 (2020) 318–326, <https://doi.org/10.1021/jacs.9b10261>.
- [38] C.E. Petoukhoff, S. Kosar, M. Goto, I. Bozkurt, M. Manish, K.M. Dani, Charge transfer dynamics in conjugated polymer/MoS<sub>2</sub> organic/2D heterojunctions, *Mol. Syst. Des. Eng.* 4 (2019) 929–938, <https://doi.org/10.1039/c9me00019d>.



- [39] J. Schneider, M. Matsuoka, M. Takeuchi, J. Zhang, Y. Horiuchi, M. Anpo, D. W. Bahnemann, Understanding TiO<sub>2</sub> Photocatalysis: Mechanisms and Materials, *Chem. Rev.* 114 (2014) 9919–9986, <https://doi.org/10.1021/cr5001892>.
- [40] Y. Zhou, W. Jiao, Y. Xie, F. He, Y. Ling, Q. Yang, J. Zhao, H. Ye, Y. Hou, Enhanced photocatalytic CO<sub>2</sub>-reduction activity to form CO and CH<sub>4</sub> on S-scheme heterostructured ZnFe<sub>2</sub>O<sub>4</sub>/Bi<sub>2</sub>MoO<sub>6</sub> photocatalyst, *J. Colloid Interface Sci.* 608 (2022) 2213–2223, <https://doi.org/10.1016/j.jcis.2021.10.053>.
- [41] T.N.Q. Trang, T.B. Phan, N.D. Nam, V.T.H. Thu, In Situ Charge Transfer at the Ag@ZnO Photoelectrochemical Interface toward the High Photocatalytic Performance of H<sub>2</sub> Evolution and RhB Degradation, *ACS Appl. Mater. Interfaces* 12 (2020) 12195–12206, <https://doi.org/10.1021/acsami.9b15578>.
- [42] Q. Pan, M. Abdellah, Y. Cao, W. Lin, Y. Liu, J. Meng, Q. Zhou, Q. Zhao, X. Yan, Z. Li, H. Cui, H. Cao, W. Fang, D.A. Tanner, M. Abdel-Hafiez, Y. Zhou, T. Pullerits, S.E. Canton, H. Xu, K. Zheng, Ultrafast charge transfer dynamics in 2D covalent organic frameworks/Re-complex hybrid photocatalyst, *Nat. Commun.* 13 (2022) 845, <https://doi.org/10.1038/s41467-022-28409-2>.
- [43] L. Collado, T. Naranjo, M. Gomez-Mendoza, C.G. López-Calixto, F.E. Oropeza, M. Liras, J. Marugán, V.A. de la Peña O'Shea, Conjugated Porous Polymers Based on BODIPY and BOPHY Dyes in Hybrid Heterojunctions for Artificial Photosynthesis, *Adv. Funct. Mater.* (2021) 2105384–2105396, <https://doi.org/10.1002/adfm.202105384>.
- [44] S. Sharma, A.O. Ibadon, M. Grazia Francesconi, S.K. Mehta, S. Elumalai, S. K. Kansal, A. Umar, S. Baskoutas, Bi<sub>2</sub>WO<sub>6</sub>/C-dots/TiO<sub>2</sub>: A novel z-scheme photocatalyst for the degradation of fluoroquinolone levofloxacin from aqueous medium, *Nanomaterials* 10 (2020), <https://doi.org/10.3390/nano10050910>.
- [45] F. Rabanimehr, M. Farhadian, A.R.S. Nazar, M. Moghadam, Fabrication of Z-scheme Bi<sub>2</sub>WO<sub>6</sub>/CNT/TiO<sub>2</sub> heterostructure with enhanced cephalexin photodegradation: Optimization and reaction mechanism, *J. Mol. Liq.* 339 (2021), 116728, <https://doi.org/10.1016/j.molliq.2021.116728>.
- [46] Y. Bai, K. Nakagawa, A.J. Cowan, C.M. Aitchison, Y. Yamaguchi, M. A. Zwiijnenburg, A. Kudo, R.S. Sprick, A.I. Cooper, Photocatalyst Z-scheme system composed of a linear conjugated polymer and BiVO<sub>4</sub>, Overall Water Split. Visible Light, *J. Mater. Chem. A* 8 (2020) 16283–16290, <https://doi.org/10.1039/d0ta04754f>.
- [47] Y. Zhang, P. Ju, L. Hao, X. Zhai, F. Jiang, C. Sun, Novel Z-scheme MoS<sub>2</sub>/Bi<sub>2</sub>WO<sub>6</sub> heterojunction with highly enhanced photocatalytic activity under visible light irradiation, *J. Alloy. Compd.* 854 (2021), 157224, <https://doi.org/10.1016/j.jallcom.2020.157224>.
- [48] Y. Jiang, H.Y. Chen, J.Y. Li, J.F. Liao, H.H. Zhang, X.D. Wang, D. Bin Kuang, Z-Scheme 2D/2D Heterojunction of CsPbBr<sub>3</sub>/Bi<sub>2</sub>WO<sub>6</sub> for Improved Photocatalytic CO<sub>2</sub> Reduction, *Adv. Funct. Mater.* (2020) 2004293–2004301, <https://doi.org/10.1002/adfm.202004293>.
- [49] J. Hu, D. Chen, Z. Mo, N. Li, Q. Xu, H. Li, J. He, H. Xu, J. Lu, Z-Scheme 2D/2D Heterojunction of Black Phosphorus/Monolayer Bi<sub>2</sub>WO<sub>6</sub> Nanosheets with Enhanced Photocatalytic Activities, *Angew. Chem. - Int. Ed.* 58 (2019) 2073–2077, <https://doi.org/10.1002/anie.201813417>.